Diagnosing Northern Hemisphere Jet Portrayal in 17 CMIP3 Global Climate Models: Twentieth-Century Intermodel Variability

SHARON C. DELCAMBRE

*Department of Atmospheric and Oceanic Sciences, and Nelson Institute Center for Climatic Research,
University of Wisconsin—Madison, Madison, Wisconsin*

DAVID J. LORENZ

Nelson Institute Center for Climatic Research, University of Wisconsin—Madison, Madison, Wisconsin

DANIEL J. VIMONT

*Department of Atmospheric and Oceanic Sciences, and Nelson Institute Center for Climatic Research,
University of Wisconsin—Madison, Madison, Wisconsin*

JONATHAN E. MARTIN

Department of Atmospheric and Oceanic Sciences, University of Wisconsin—Madison, Madison, Wisconsin

(Manuscript received 12 June 2012, in final form 27 January 2013)

ABSTRACT

The present study focuses on diagnosing the intermodel variability of nonzonally averaged NH winter jet stream portrayal in 17 global climate models (GCMs) from phase three of the Coupled Model Intercomparison Project (CMIP3). Relative to the reanalysis, the ensemble-mean 300-hPa Atlantic jet is too zonally extended and located too far equatorward in GCMs. The Pacific jet varies significantly between modeling groups, with large biases in the vicinity of the jet exit region that cancel in the ensemble mean. After seeking relationships between twentieth-century model wind biases and 1) the internal modes of jet variability or 2) tropical sea surface temperatures (SSTs), it is found that biases in upper-level winds are strongly related to an ENSO-like pattern in winter-mean tropical Pacific Ocean SST biases. The spatial structure of the leading modes of variability of the upper-level jet in the twentieth century is found to be accurately modeled in all 17 GCMs. Also, it is shown that Pacific model biases in the longitude of EOFs 1 and 2 are strongly linked to the modeled longitude of the Pacific jet exit, indicating that the improved characterization of the mean state of the Pacific jet may positively impact the modeled variability. This work suggests that improvements in model portrayal of the tropical Pacific mean state may significantly advance the portrayal of the mean state of the Pacific and Atlantic jets, which will consequently improve the modeled jet stream variability in the Pacific. To complement these findings, a companion paper examines the twenty-first-century GCM projections of the nonzonally averaged NH jet streams.

1. Background

A poleward shift of the jet streams under anthropogenic climate change has been theorized (Chen and Held 2007; Lorenz and DeWeaver 2007; Kidston et al. 2011) and observed over the past 30 years (Thompson and Wallace 2000; Marshall 2003; Hu et al. 2007; Johanson and Fu 2009) and is broadly expected to continue into the future (Solomon et al. 2007). Despite the multitude of studies acknowledging this poleward shift, jet stream winds still vary significantly among observational datasets and various model simulations. The present study contributes a detailed analysis of global climate model (GCM) portrayal of jet stream structure and variability in twentieth-century simulations as the precursor to a second study (Delcambre et al. 2013) that will analyze twenty-first-century GCM projections of jet stream portrayal.

Jet streams are closely related to storm frequency and intensity across the midlatitudes and a small change in jet position or intensity significantly impacts the weather experienced by a large fraction of the world's population. Also, it is important that GCMs correctly model the large-scale circulation (of which the jet stream is a primary feature) in order to gain confidence in other variables that may be controlled by the large-scale circulation such as precipitation over North America related to the Pacific storm track. A careful examination of previous work on this topic reveals that many studies infer jet position based upon the poleward extent of the Hadley cell, the phase of the hemispheric annular mode, or the position of midlatitude storm tracks.

The poleward boundaries of the Hadley cell effectively represent the latitudinal extent of the tropical atmosphere and are coincident with the locations of the subtropical jets. Observational studies exploring a variety of reanalysis and outgoing longwave radiation (OLR) datasets show that a 2°–4.5° latitude expansion of the Hadley cell has occurred between 1979 and 2005 (Hu et al. 2007). While this time period may not be long enough to distinguish a long-term trend from decadal variability, this observed widening does not seem to be explained by internal atmospheric variability, which is less than 1.5° latitude in preindustrial GCM experiments (Johanson and Fu 2009). GCMs project even more poleward expansion of the Hadley cell in the future, averaging to a 2° latitude expansion by the end of the twenty-first century (Lu et al. 2007). This estimate is much smaller than what has already been observed, suggesting that either the subtropical jet will translate poleward under anthropogenic climate change more than estimates by GCMs suggest or that much of the observed ''trend'' is a result of internal variability.

While the Hadley cell is used as a proxy for the subtropical jet, the northern and southern annular modes (NAM and SAM; also called the Arctic and Antarctic Oscillation) describe a north–south shift of mass between the midlatitudes and the poles, describing a north–south shift of the polar (i.e., eddy driven) jets (Thompson and Wallace 2000). In addition, NAM and SAM are the dominant modes of hemispheric climate variability at all levels, making the annular mode a convenient and useful proxy for describing polar jet stream translations. In agreement with other measures of jet stream position, the observed NAM and SAM have trended positive over the latter half of the twentieth century, indicating the occurrence of a poleward shift of the polar jet in both hemispheres (Thompson et al. 2000; Marshall 2003). However, the magnitude of this trend is currently in question because the annular mode has become significantly less positive since 2000 (Overland and Wang

2005). Also, a recent study suggests that using the sea level NAM/SAM, as is common practice, is ineffectual to describe jet shifts because it does not take into account the baroclinic structure of the anthropogenic climate change signal (Woollings 2008). Despite this uncertainty, future projections of the NAM/SAM are certainly important. In fact, intermodel variance of the NAM in climate projections is shown to be responsible for up to 40% of surface temperature and precipitation variance over Eurasia and North America in late-twenty-first-century projections (Karpechko 2010).

The more common proxy for polar jet stream position is the mean position of midlatitude storm tracks, which are dynamically tied to polar jet stream position and intensity (Valdes and Hoskins 1989; Orlanski 1998; Chang et al. 2002). Storm tracks, which are predominantly located on the downstream and poleward side of the polar jets, are well replicated in GCMs using both feature-tracking algorithms and statistical metrics (Hoskins et al. 1983; Hoskins and Valdes 1990; Hodges 1994; Bengtsson et al. 2006; Ulbrich et al. 2008). However, interpreting future projections of storm-track position is much more difficult. While some studies find that modeled storm tracks shift poleward by the end of the twenty-first century (Yin 2005), other studies suggest a poleward expansion and intensification of future storm tracks (Wu et al. 2010). In general, the projected poleward shift of Southern Hemisphere (SH) storm tracks is much clearer and more robust than the shift of storm tracks in the Northern Hemisphere (NH), which are fraught with model discrepancies (Bengtsson et al. 2006; Ulbrich et al. 2008).

The few studies that look directly at jet stream winds have also lacked consensus with regard to modeled future jet stream structure, especially in the Northern Hemisphere. While the World Climate Research Programme's (WCRP's) phase 3 of the Coupled Model Intercomparison Project (CMIP3) multimodel dataset (Meehl et al. 2007) ensemble mean shows a poleward shift and intensification of zonal-mean winds (Kushner et al. 2001; Lorenz and DeWeaver 2007), the intermodel spread is larger than the ensemble mean, reducing confidence in GCM projections (Kidston and Gerber 2010; Woollings and Blackburn 2012). Overall, low-level (such as 850 mb or 10 m) wind speeds are more consistent between modeling groups, perhaps indicating that the polar eddy-driven jet—which penetrates into the lower troposphere, unlike the subtropical jet—has a clearer response to anthropogenic climate change (Woollings and Blackburn 2012). Adding complexity to the situation, all CMIP3 GCMs have been found to position the zonal-mean jet too far equatorward in both hemispheres in the twentieth century when compared with

reanalysis data (Kidston and Gerber 2010; Woollings and Blackburn 2012).

Because of the possible differences between subtropical and polar jet responses to anthropogenic climate change, studies that do not use a zonal-mean perspective have found distinct results for different local jet stream structures. For instance, one recent observational study has shown that the NH Atlantic jet has shifted northward while the NH Pacific (East Asian) jet has not (Yaocun and Daqing 2011). Even on a regional scale, however, the variations among GCM portrayals of jet stream structure are significant. A sectorial study of the zonal-mean NH Atlantic and Pacific regions in 23 GCMs finds that while the intensification of upper-level winds is consistent in GCMs, a poleward shift of jet stream winds varies widely among modeling groups (Ihara and Kushnir 2009).

Because twenty-first-century projections of jet stream structure are correlated with twentieth-century jet model biases (Kidston and Gerber 2010), the next step toward understanding future jet stream structure is a careful analysis of twentieth-century model biases, as presented in this paper. The goal of this study is to understand why there is a lack of model consensus of NH jet structure in twentieth-century simulations. A follow-up study will then discuss how to use this knowledge of twentieth-century simulations to better understand twenty-first-century projections. While analyses of the zonal-mean wind are a good starting point for an examination of the large-scale circulation, this study goes one step further to look at the upper-level winds separately for the Atlantic and Pacific basins without the use of zonal averaging. This type of analysis is valuable because of the complex jet dynamics associated with the asymmetric NH circulation. It also adds insight into the potential mechanisms that underlie a poleward shift of the jet stream, as will be discussed in much greater depth in the second part of this study.

The present paper is organized as follows. Section 2 outlines the reanalysis and GCM data used in this study. Results of a detailed comparison between GCM simulations and reanalysis are presented in section 3. These results include the analysis of ensemble-mean winter biases as well as an examination of intermodel variations and the portrayal of jet stream variability in GCMs. Conclusions are found in section 4.

2. Data and methods

In this study, reanalysis data are used to establish a climatology of NH jet streams based upon the 1962–2000 winter-mean zonal winds (winters are labeled according to the year corresponding with January). These data come from the National Centers for Environmental Prediction (NCEP)–National Center for Atmospheric Research (NCAR) Reanalysis 1 dataset (Kalnay et al. 1996). To determine the accuracy of jet stream characterization in each model, 17 GCMs are assessed in comparison with the reanalysis. They come from the WCRP's CMIP3 multimodel dataset for the climate of the twentieth-century experiment (20C3M) (Meehl et al. 2007). Table 1 lists the CMIP3 models included in this study and provides expansions of model names. These particular models are chosen because they provide the daily-resolved data required for this study. It is very likely that different modeling centers made substantially different assumptions regarding spinup from control as well as the amplitude and timing of anthropogenic and natural forcing. In this study, no attempt is made to separate the contribution of this external forcing from the intermodel variability caused by model physics.

The present study employs daily 300-hPa zonal wind data and monthly sea surface temperature (SST) data for 20 boreal winter seasons. A complementary analysis using 700-hPa zonal wind data (not discussed) is found to be in close agreement with the results at 300 hPa, suggesting that the current analysis incorporates both subtropical and polar jet variability.

Daily wind data are smoothed using a 5-day running mean for the period encompassing 1 November–31 March of each winter from November 1961 to March 2000 (with leap days removed). The 17 GCMs vary in resolution from $1.125°$ latitude $\times$ $1.125°$ longitude (model 1, INGV-SXG) to $4°$ latitude $\times$ $5°$ longitude (model 17, INM-CM3.0). To directly compare model and reanalysis data, each model is linearly interpolated to $2.5°$ latitude $\times$ $2.5°$ longitude resolution. Resolution differences between models are not found to be related to the accuracy of jet stream portrayal.

To create the winter-mean zonal wind, the smoothed (5-day running mean) data are averaged over November–March (NDJFM) and over all 20 years of the data period. To create the winter-mean SST, the monthly data are averaged over the same period. The seasonal cycle of zonal wind is created by averaging each smoothed day (i.e., pentad) over all 39 boreal winter seasons. Daily wind data (with the seasonal cycle removed) are used to perform empirical orthogonal function (EOF)/principal component (PC) analysis.

3. Results and discussion

a. Jet portrayal in NCEP–NCAR reanalysis

Both the mean state and variability of the upper-level winds are examined in order to gain a full understanding

TABLE 1. CMIP3 models and expansions of model names.

Number	Model	Modeling group	Reference
1	INGV Scale Interaction Experiment (SINTEX-G) (INGV-SXG)	Instituto Nazionale di Geofisica e Vulcanologia (INGV)	Gualdi et al. (2006, 2008)
2	Model for Interdisciplinary Research on Climate, version 3.2 (high resolution) [MIROC3.2 (hires)]	Center for Climate System Research (the University of Tokyo), National Institute for Environmental Studies, and Frontier Research Center for Global Change [Japan Agency for Marine-Earth Science and Technology (JAMSTEC)]	Hasumi and Emori (2004)
3	CSIRO Mark, version 3.0 (CSIRO Mk3.0)	Commonwealth Scientific and Industrial Research Organisation (CSIRO)	Gordon et al. (2002)
4	CSIRO Mark, version 3.5 (CSIRO Mk3.5)	CSIRO	Gordon et al. (2002)
5	ECHAM5/MPI Ocean Model (MPI-OM)	Max Planck Institute for Meteorology (MPI)	Jungclaus et al. (2006)
6	GFDL Climate Model, version 2.0 (GFDL CM2.0)	U.S. Department of Commerce/National Oceanic and Atmospheric Administration (NOAA)/Geophysical Fluid Dynamics Laboratory (GFDL)	Delworth et al. (2006) and Gnanadesikan et al. (2006)
7	BCCR Bergen Climate Model, version 2.0 (BCCR-BCM2.0)	Bjerknes Centre for Climate Research (BCCR)	http://www.bjerknes.uib.no/
8	CCCma Coupled Global Climate Model, version 3.1 (T63 resolution) [CGCM3.1 (T63)]	Canadian Centre for Climate Modelling and Analysis (CCCma)	Flato et al. (2000), (http://www.ec.gc.ca/ccmac-cccma)
9	CNRM Coupled Global Climate Model, version 3 (CNRM-CM3)	Météo-France/Centre National de Recherches Météorologiques (CNRM)	http://www.cnrm.meteo.fr/scenario2004/paper_cm3.pdf
10	MIROC3.2, (medium resolution) [MIROC3.2 (medres)]	Center for Climate System Research (the University of Tokyo), National Institute for Environmental Studies, and Frontier Research Center for Global Change (JAMSTEC)	Hasumi and Emori (2004)
11	MRI Coupled Atmosphere–Ocean General Circulation Model, version 2.3.2 (MRI-CGCM2.3.2)	Meteorological Research Institute (MRI)	Yukimoto et al. (2006)
12	Flexible Global Ocean–Atmosphere–Land System Model gridpoint, version 1.0 (FGOALS-g1.0)	National Key Laboratory of Numerical Modeling for Atmospheric Sciences and Geophysical Fluid Dynamics (LASG)/Institute of Atmospheric Physics (IAP)	Yu et al. (2002, 2004)
13	CGCM3.1 (T47 resolution) [CGCM3.1 (T47)]	CCCma	Flato et al. (2000), (http://www.ec.gc.ca/ccmac-cccma)
14	Max Planck Institut für Meteorologie (MPI)	Meteorological Institute of the University of Bonn, Meteorological Research Institute of KMA, and Model and Data group	http://www-pcmdi.llnl.gov/projects/modeldoc/cmip/echo-g_tbls.html
15	GISS Atmosphere–Ocean Model (GISS-AOM)	National Aeronautics and Space Administration (NASA) Goddard Institute for Space Studies (GISS)	Russell et al. (1995) and Lucarini and Russell (2002)
16	GISS Model E, coupled with the Russell ocean model (GISS-ER)	NASA GISS	Schmidt et al. (2006)
17	INM Coupled Model, version 3.0 (INM-CM3.0)	Institute of Numerical Mathematics (INM)	Volodin and Diansky (2004) and Galin et al. (2003)

of the NH jet streams in reanalysis data, which is then used to assess GCM accuracy. The reanalysis winter-mean 300-hPa zonal wind for 1962–2000 (using winter-averaged filtered daily data) is shown in Fig. 1, with wind speed maxima located in the Pacific and Atlantic basins (hereafter called the Pacific and Atlantic jets). The Pacific jet extends from East Asia across the Pacific basin and the Atlantic jet extends from the central continental United States to the western coast of Europe, tilting northeastward across the Atlantic basin.

The dominant modes of variability of the reanalysis are identified with EOF/PC analysis of the daily 300-hPa zonal wind field with the seasonal cycle removed. EOF/PC analysis is performed on the area-weighted reanalysis
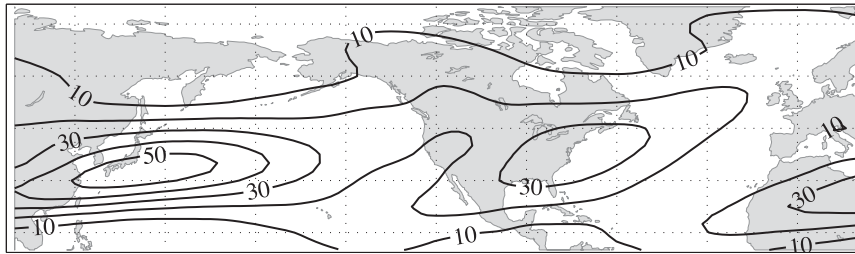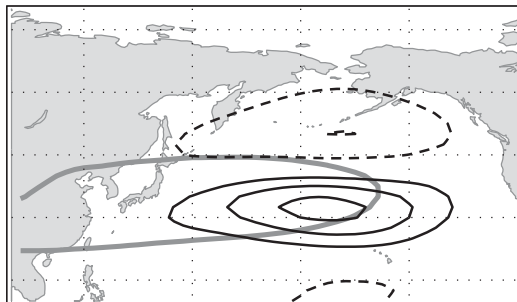
FIG. 1. NH reanalysis zonal wind [m s^{-1}; contour interval (CI): 10 m s^{-1}] at 300 hPa for NDJFM during 1962–2000.

data over the North Atlantic (22.5°–80°N, 120°W–20°E) and the North Pacific (22.5°–80°N, 100°E–120°W) basins for winter (NDJFM) during 1962–99. All PCs are normalized to unit variance and all EOFs/PCs shown in this study have been found to be well separated from higher-order EOFs/PCs as determined by the methodology of North et al. (1982). The two dominant modes of variability for each basin are shown in Fig. 2 as regressions of the 300-hPa zonal wind field (0°–80°N) onto the first and second PCs of the zonal wind.

In the Pacific, the primary mode of variability explains 20% of the variance in the upper-level zonal wind, with the dominant variant structure (i.e., zonal

wind anomaly) located near the jet exit region (Fig. 2a), indicating a strengthening and weakening of zonal winds in this region. This mode represents a downstream extension or retraction of the upper-level jet (Jaffe et al. 2011). The secondary mode of variability in the Pacific explains 13% of the variance in the upper-level zonal wind and looks quite different from the primary mode of variability, with a dipole of variant structures straddling the jet axis near the jet exit region (Fig. 2b). This pattern represents a north-/southward shift of the jet near the exit region. The tertiary mode of variability (not shown) explains 11% of the variance in the upper-level zonal wind.
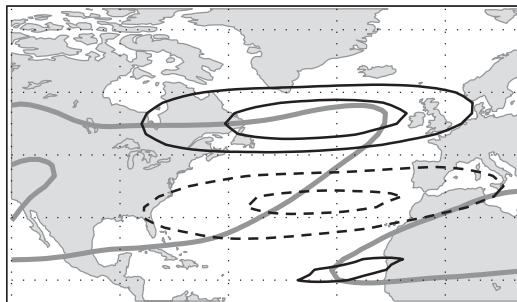
a. EOF 1 (Extend/Retract) − 20% Var. Expl.   b. EOF 2 (Shift) − 13% Var Expl.
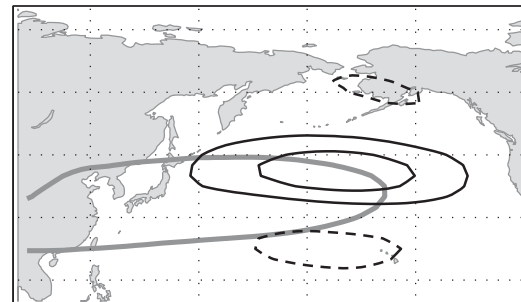
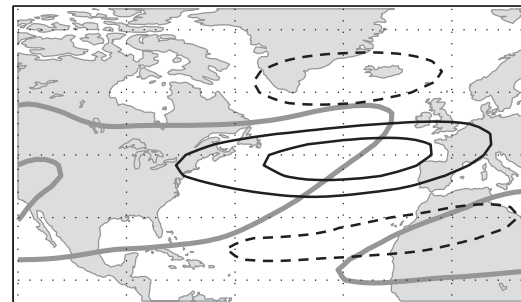c. EOF 1 (Shift) − 20% Var. Expl.   d. EOF 2 (Extend/Retract) − 16% Var. Expl.

FIG. 2. EOFs of the 300-hPa midlatitude zonal wind field (20°–80°N) regressed onto the total 300-hPa zonal wind field (0°–80°N) for: (a) Pacific basin EOF 1 (extend/retract), (b) Pacific basin EOF 2 (shift), (c) Atlantic basin EOF 1 (shift), and (d) Atlantic basin EOF 2 (extend/retract) (contoured every 4 m s^{-1} with zero line removed). Solid (dashed) black lines represent positive (negative) perturbation isotachs and gray contours show the 20 (30) m s^{-1} isotach of the mean 300-hPa zonal wind for the Atlantic (Pacific) basins, as in Fig. 1.

In the Atlantic, the first mode of variability (20% of the total variance) resembles a north-/southward shift of the eastern half of the jet (Fig. 2c) and the second mode of variability (16% of the total variance) characterizes a strengthening/weakening of the zonal wind speeds in the jet core especially in the eastern half of the jet (Fig. 2d). The third mode of variability (not shown) explains 10% of the total variance. Because the structure of the Atlantic jet includes a southwest–northeast-oriented tilt from southeastern North America toward the British Isles, an additional level of complexity is added to the interpretation of these patterns of variability. To be certain of the correct interpretation, a composite analysis is performed, averaging over the smoothed daily data that have PCs 1–2 greater than one standard deviation (or less than minus one standard deviation). This threshold includes the pentads with the largest magnitude variability of the upper-level winds. The composite winds for each case are shown in Fig. 3. These results support the interpretation that the primary mode of variability of the Atlantic jet is more like a north-/southward shift and the secondary mode of variability is more like a strengthening/weakening of the jet exit region. The north-/southward shift of the jet can be seen by comparing positive EOF 1 in Fig. 3a with negative EOF 1 in Fig. 3b and the extension/retraction of the jet can be seen by comparing positive EOF 2 in Fig. 3c with negative EOF 2 in Fig. 3d. The composite retraction of the Atlantic jet (Fig. 3d) appears to be related to a blocking ridge over southwestern Europe, which is the main feature that differs between positive and negative EOF 2 polarity. It is likely that the characteristic split jet structure of negative EOF 2 is related to Atlantic blocking. The dominant modes of variability of the Pacific and Atlantic jets shown in Figs. 2 and 3 are consistent with many previous studies, including Simmons et al. (1983), Athanasiadis et al. (2010), Wettstein and Wallace (2010), Woollings et al. (2012b), and Li and Wettstein (2012).

Although the two leading modes of variability in the Pacific and Atlantic basin are opposite one another, they can be interpreted similarly. To add meaning to the discussion of these modes of variability they will be referred to as the "shift EOF" (Pacific EOF 2 and Atlantic EOF 1) and "extend/retract EOF" (Pacific EOF 1 and Atlantic EOF 2) throughout the remainder of the paper. It has been suggested that the reversal of the primary and secondary modes of variability between the Pacific and Atlantic jets results from differences in the orientation of the subtropical and eddy-driven jets in the two regions (Eichelberger and Hartmann 2007). This is likely related to the distinct nature of the jet in each region, with the upper-level winds in the Pacific dominated by the
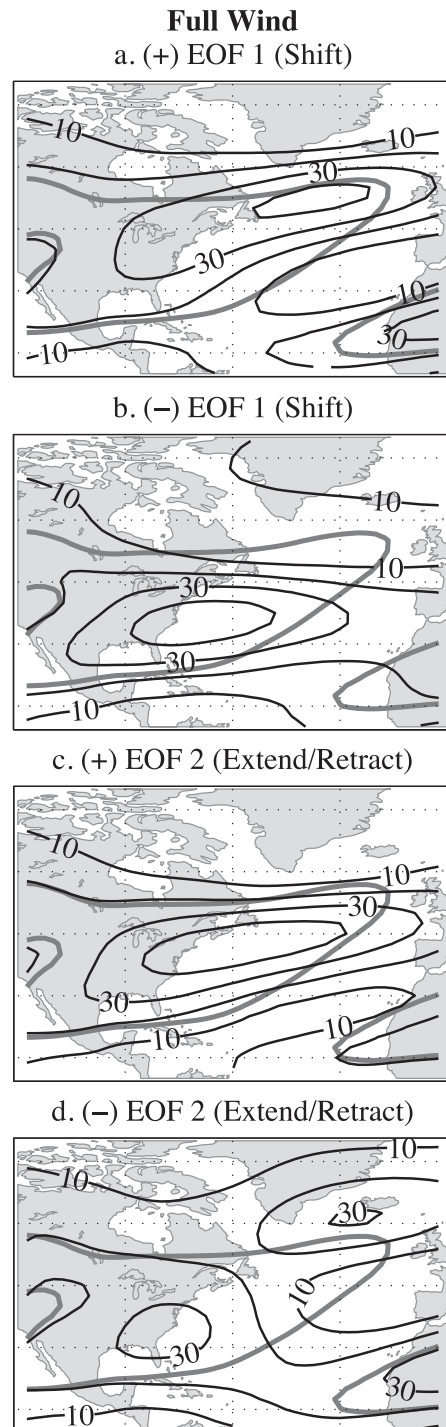
Full Wind

a. (+) EOF 1 (Shift)

b. (−) EOF 1 (Shift)

c. (+) EOF 2 (Extend/Retract)

d. (−) EOF 2 (Extend/Retract)

FIG. 3. Composites of max variability of the 300-hPa zonal wind field $(m\,s^{-1})$ in the Atlantic. Black lines represent perturbation isotachs added to the climatology and gray contours show the $20\,m\,s^{-1}$ isotach of the mean 300-hPa zonal wind for the Atlantic for: (a) first PC greater than one std dev (1σ), (b) first PC less than -1σ, (c) second PC greater than 1σ, and (d) second PC less than -1σ.

a. Ensemble Mean Bias
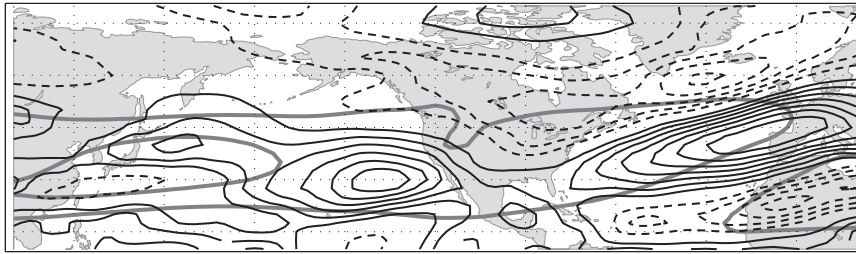
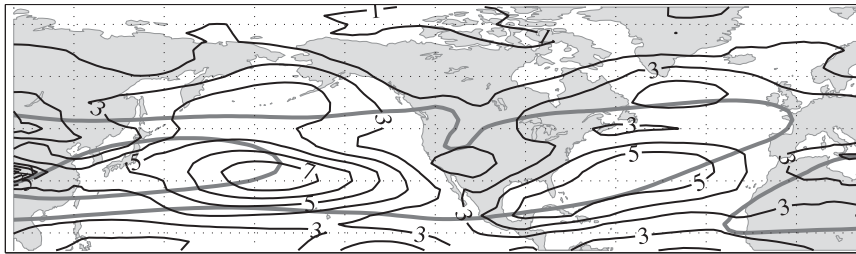b. Model Standard Deviation of Bias

FIG. 4. (a) Ensemble-mean model bias and (b) standard deviation of models about the ensemble mean for the 17 GCMs under consideration (contoured every $1\,\mathrm{m\,s^{-1}}$ with zero line removed). Solid (dashed) black contours in (a) represent positive (negative) values of ensemble-mean bias. Gray contours show the 20 and $40\,\mathrm{m\,s^{-1}}$ isotachs of the model winter-mean 300-hPa zonal wind.

influence of the subtropical jet stream, and the upper-level winds in the Atlantic influenced by both the polar and subtropical jet streams (Lorenz and Hartmann 2003; Eichelberger and Hartmann 2007). Valuable insights about the differences between these two regions can be gained through a nonzonally averaged analysis of the NH jets (Athanasiadis et al. 2010; Woollings et al. 2012b).

b. GCM bias of the winter-mean jet

Model bias is defined to be the difference between the GCM and reanalysis smoothed daily 300-hPa zonal wind ($U_{\mathrm{bias}} = U_{\mathrm{GCM}} - U_{\mathrm{reanalysis}}$). A positive model bias indicates that modeled zonal wind speeds are too high in a given location and negative model bias shows where modeled zonal wind speeds are too low. Figure 4a shows the average winter model bias for the 17 GCMs being considered. Overall, model bias of the upper-level zonal wind is on the same order of magnitude as the two dominant modes of variability seen in Fig. 2. Also, the amplitude of the average model bias is of the same order of magnitude as the standard deviation of model bias around the ensemble mean (Fig. 4b).

The largest bias of the model mean occurs in the Atlantic, where the jet is too extended and positioned too far equatorward on average in the models. The modeled jet is also positioned too far equatorward in the Southern Hemisphere (not shown), supporting the results of

Kidston and Gerber (2010). The bias of the model mean in the Atlantic is somewhat larger than the standard deviation about the ensemble mean, indicating that biases are fairly consistent across models in this basin. The standard deviation for the Atlantic jet is positioned farther west than the model-mean bias, with two maxima located on the pole- and equatorward flanks of the Atlantic jet.

Relative to the Atlantic, the bias of the model mean is small in the Pacific, with one isolated region of positive bias in the eastern Pacific and another weak region of positive bias on the poleward flank of the Pacific jet. However, the standard deviation of models about the ensemble mean is quite large, indicating that individual models exhibit much variability in their portrayal of the mean Pacific jet. This means that the ensemble mean improves upon the ability of individual models to reproduce the Pacific jet. The standard deviation is largest, more than $8\,\mathrm{m\,s^{-1}}$, in the Pacific jet exit region, strongly resembling the dominant mode of Pacific pentad variability (EOF 1—extension/retraction) in the NCEP–NCAR reanalysis (Fig. 2a).

An examination of individual model portrayals of the winter-mean jets (representative examples shown in Fig. 5) shows that some models have very small biases (Figs. 5a,b) while other models have bias patterns that resemble the dominant modes of variability of the observed winter jet (Figs. 5c–f).
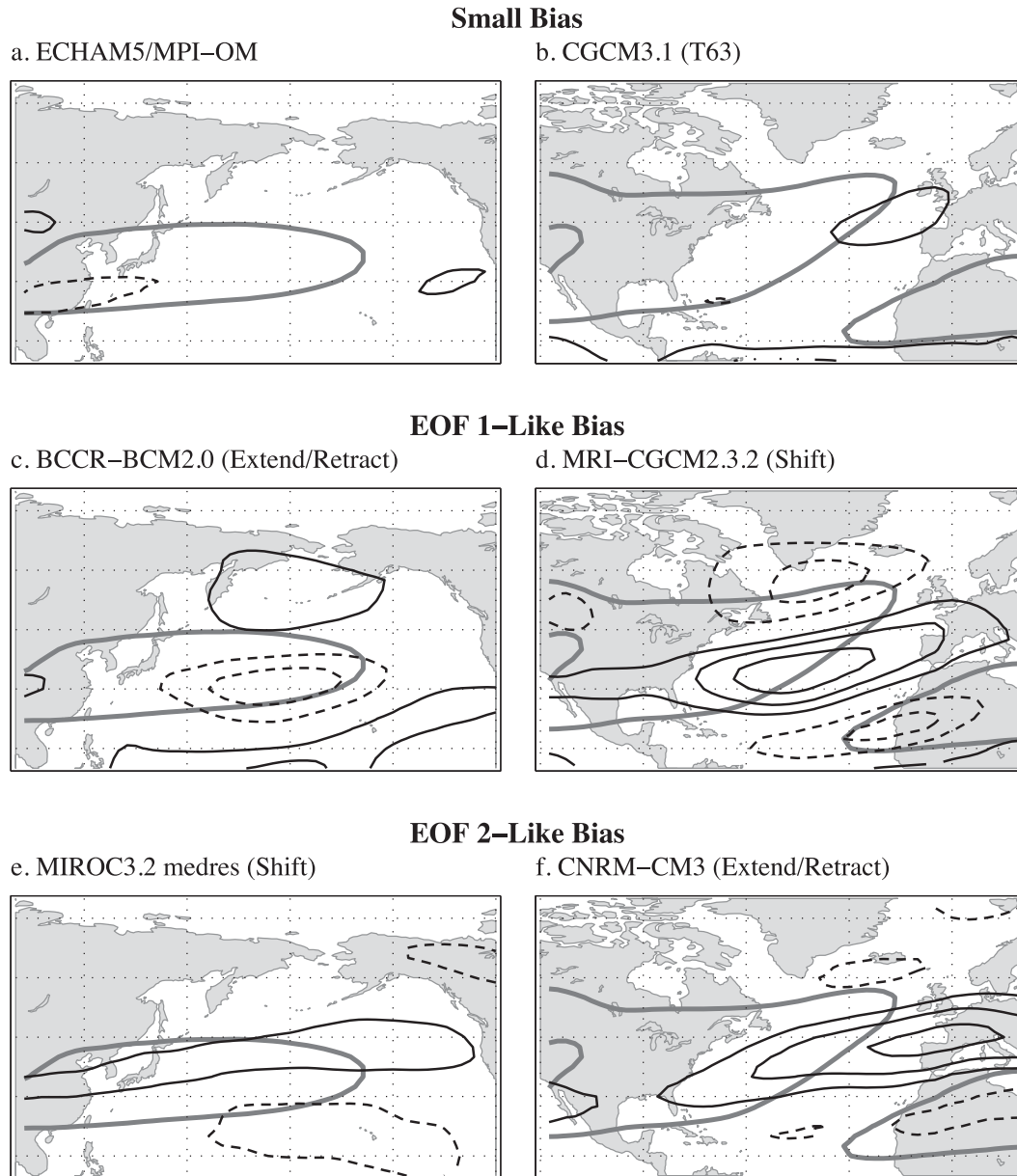
Small Bias

a. ECHAM5/MPI−OM

b. CGCM3.1 (T63)

EOF 1−Like Bias

c. BCCR−BCM2.0 (Extend/Retract)

d. MRI−CGCM2.3.2 (Shift)

EOF 2−Like Bias

e. MIROC3.2 medres (Shift)

f. CNRM−CM3 (Extend/Retract)

FIG. 5. Solid (dashed) black contours show the positive (negative) bias of the 300-hPa zonal wind (contoured every $4 \, \text{m s}^{-1}$ with zero line removed) and gray contours show the 20 (30) m s^{-1} isotachs of the reanalysis 300-hPa zonal wind in the Atlantic (Pacific) for: (a) model 5, ECHAM5/MPI-OM; (b) model 8, CGCM3.1 (T63); (c) model 7, BCCR-BCM2.0; (d) model 11, MRI-CGCM2.3.2; (e) model 10, MIROC3.2(medres); and (f) model 9, CNRM-CM3.

As a first step toward understanding the cause of model biases, it is important to determine the relationship of these biases with the dominant modes of variability in the Pacific and Atlantic regions. Such relationships offer clues that help explain the existence of model biases by condensing this large amount of data into a two-dimensional analysis that shows the similarities and differences among models. A normalized projection of each model's area-weighted winter-mean bias onto the area-weighted first and second EOFs of the upper-level zonal wind from the reanalysis (shown in Fig. 2) is used to quantify the relationship between the model biases and the observed modes of jet variability. "Normalized" signifies that the projection of each model's bias onto reanalysis EOFs 1 and 2 is divided by the magnitude of both the respective model bias and EOF pattern. The normalized projection is similar to a spatial correlation except that in the former the spatial mean has not been

removed. This analysis is done separately for the Atlantic (120°W–20°E) and Pacific (100°E–120°W) basins and results are shown in Fig. 6. The sign convention used for the patterns of the reanalysis EOFs 1 and 2 is that shown in Fig. 2. The position of each point with respect to the x axis shows the value of each model's projection onto EOF 1 from the reanalysis and the position of each point with respect to the y axis shows the value of each model's projection onto reanalysis EOF 2.

In the Pacific, the projection of each model's bias onto the dominant modes of variability from the reanalysis (Fig. 6a) shows two clusters of models, with one on the positive side of the x axis and the other on the negative side of the x axis. The first group of models (group 1, depicted with crosses) has biases clustered on the negative x axis, indicating their similarity to a retraction of the Pacific jet (negative EOF 1). The second group of models (group 2, depicted with asterisks) has biases clustered on the positive x axis, indicating their similarity to an extension of the Pacific jet (positive EOF 1). The means of groups 1 and 2 are found to be statistically different at 99% confidence using a bivariate t test. It is important to note that despite the separation in the space of EOFs 1 and 2, the lengths of the normalized projections are only ∼0.5–0.6, indicating that EOFs 1 and 2 are not complete in their explanation of jet bias. The black line connects the average group 1 projection to the average group 2 projection, and indicates an axis in the space of EOFs 1 and 2 that distinguishes group 1 from 2. The open circles and diamonds represent jet variations associated with El Niño–Southern Oscillation (ENSO)-like SST structures in the tropical Pacific and will be explained in section 3c. For our purposes here, we point out that the open circles and diamonds are parallel to the group 1/group 2 axis (solid black line); we will suggest in section 3c that this indicates that the group 1/group 2 separation is explained via ENSO-like SST structures in the tropical Pacific.

In the Atlantic (Fig. 6b), models biases are more uniform, without the distinctive two-group structure found for the Pacific. Atlantic model biases mostly cluster in quadrant 2, resembling both an extension and southward shift of the Atlantic jet (negative EOF 1 and positive EOF 2). In Fig. 6b, models continue to be depicted with crosses and asterisks according to their respective groups as determined for the Pacific—yet a delineation is still apparent between groups 1 and 2 (also found to be significant to 99% confidence using a bivariate t test). This delineation is shown by the fact that the crosses and asterisks barely overlap despite the fact that they are all located in the vicinity of quadrant 2 in Fig. 6b. The fact that this grouped bias structure holds true in the Atlantic suggests that despite the differences between the two
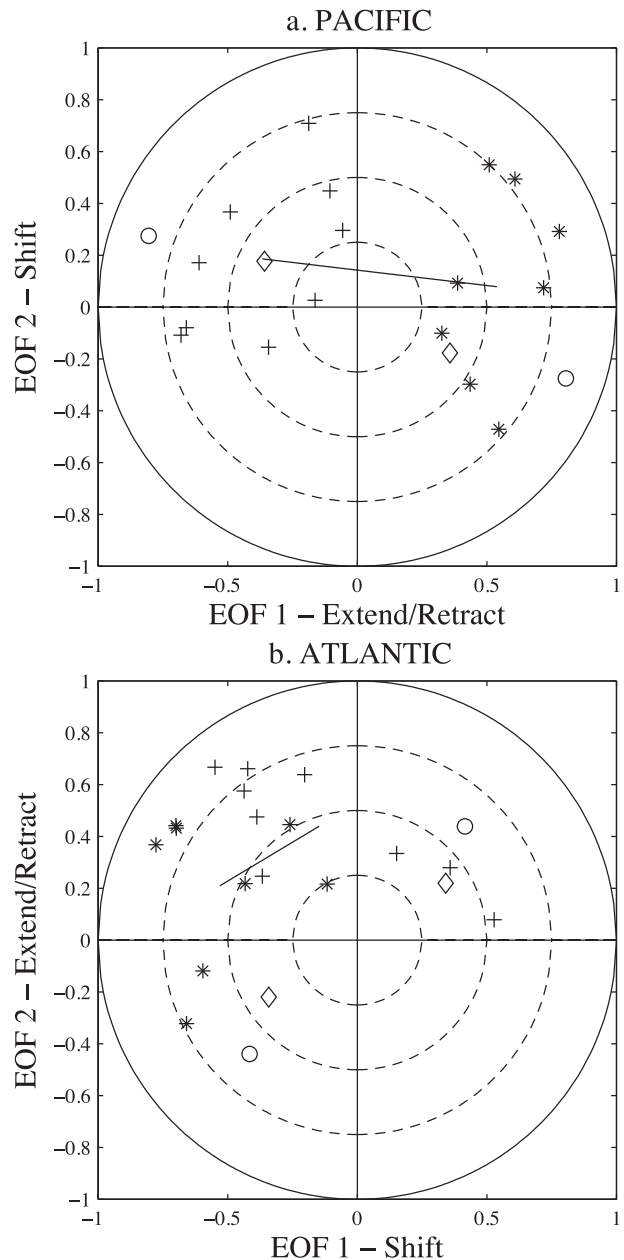

FIG. 6. Normalized projection of the model bias of the 300-hPa zonal wind onto EOFs 1 and 2 from the reanalysis for the (a) Pacific and (b) Atlantic basins. Models designated by crosses (+) are part of group 1 and models designated by asterisks (*) are part of group 2. Dashed circles indicate lines of constant correlation at $r = 0.25, 0.5,$ and 0.75. The black line connects the average group 1 projection to the average group 2 projection. Open circles (diamonds) show the values of the normalized projection of the heterogeneous wind pattern shown in Fig. 8a (ENSO teleconnection pattern shown in Fig. 9a) onto EOFs 1 and 2 (note that Figs. 8 and 9 are described in greater detail below).
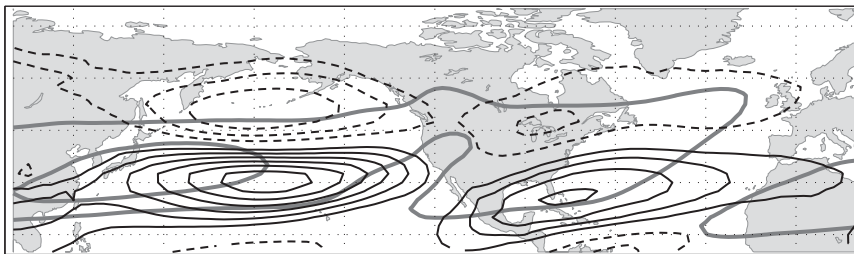
FIG. 7. Solid (dashed) black lines show the positive (negative) model bias of the 300-hPa zonal wind (contoured every $1 \, \mathrm{m \, s^{-1}}$ with zero line removed) (group 2 − group 1). Gray contours show the 20 and $40 \, \mathrm{m \, s^{-1}}$ isotachs of the model-mean 300-hPa zonal wind. Group 1 consists of models 1, 5, 7, 8, 9, 10, 12, 13, and 17. Group 2 consists of models 2, 3, 4, 6, 11, 14, 15, and 16. This is based upon their delineation in Fig. 6, as described in the text.

basins, model biases in the Atlantic and Pacific regions are likely linked.

Another way to interpret Fig. 6 is through the relationship of the Pacific and Atlantic jets as interpreted by EOFs 1 and 2 for groups 1 and 2. For instance, in the Pacific it is possible that a stronger, sharper subtropical jet (group 2) is related to a weak polar/midlatitude jet and there are relatively equal and opposite jet shifts around the mean jet position. Correspondingly, a weak or diffuse subtropical jet (group 1) could lead to a more vigorous polar/midlatitude jet and a slight poleward-shifted jet relative to the climatology. Similarly, an extended Pacific jet (group 2) is generally associated with an equatorward-shifted Atlantic jet.

To uncover the difference in spatial structure between groups 1 and 2, the model-mean bias of each group is calculated. The difference between groups 1 and 2 (group 2 − group 1) is shown in Fig. 7. There are two maxima, which indicate differences between groups 1 and 2. The first (and largest) maximum in bias difference is found in the Pacific jet exit region, in the same location as the large value of the standard deviation of model bias shown in Fig. 4b. The second maximum in bias difference is found on the southern flank of the Atlantic jet, also found in a location of high standard deviation of model bias, as shown in Fig. 4b. No significant difference between groups 1 and 2 is found in the Southern Hemisphere (not shown)

c. Relationship between jet bias and tropical Pacific SST bias in GCMs

The probable link between biases in the Pacific and Atlantic basins (despite different jet dynamics in each region) suggests that a forcing external to the midlatitude eddy/jet system is involved in producing these model biases. Because of the far-reaching influence of tropical Pacific SST variations (e.g., ENSO), this region will be considered as a possible influence on model

biases of midlatitude upper-level winds. This potential relationship will be examined using maximum covariance analysis (MCA).

MCA is used here to assess the dominant patterns of covariability between tropical SST biases and upper-level zonal wind biases in the same models. This technique identifies pairs of patterns that maximize the squared covariance between two variables: in this case the winter-average midlatitude 300-hPa zonal wind (10°–80°N, 100°E–20°W) and the winter-average tropical Pacific SST (30°S–30°N, 120°–290°E). The covariance is identified across a given sampling dimension. Typically sampling is performed across time, but in this case sampling is done across the 17 GCMs to identify structures linked to model bias. Further explanation of MCA may be found in Bretherton et al. (1992), Wallace et al. (1992), and Deser and Timlin (1997). It is important to note that because this MCA analysis samples across model space instead of across time, ENSO-like SST patterns that are identified are not equivalent to interannual variability in any model. Instead, these ENSO-like patterns of SST show the winter mean state of the tropical Pacific that is associated with a given mode of intermodel covariability.

The first mode of covariability between the wind and SST explains 55% of the total squared covariance between the two fields. Considering that the second and third modes of covariability explain 15% and 14% of the total covariance respectively, the first mode is clearly dominant. Confirming the validity of this technique, the normalized root-mean-square covariance (NRMSC) is calculated to be 0.31, meaning that there is a significant amount of total covariance between these two fields. In addition, the correlation between the two expansion coefficients (i.e., the left and right singular vectors) is 0.81, verifying that there is a high degree of coupling between the patterns identified in the wind and SST fields. A scatterplot of the SST and zonal wind expansion

a. Heterogeneous − UWND
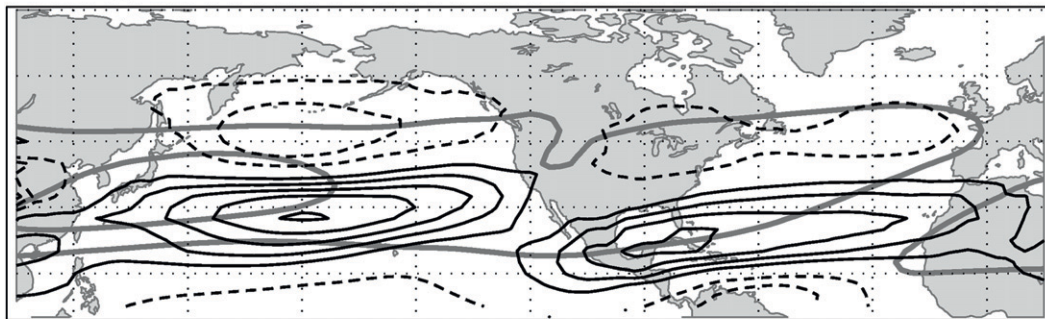
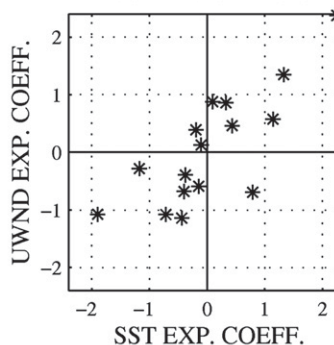## b. Homogeneous − SST
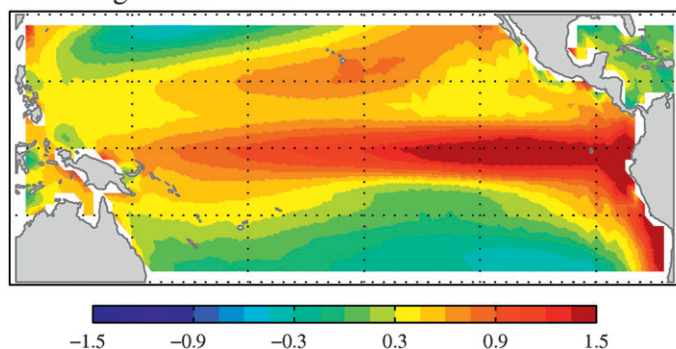
c. Correlation = 0.81

FIG. 8. Results of MCA of tropical Pacific SSTs and midlatitude 300-hPa zonal wind. (a) Heterogeneous wind regression map. Solid (dashed) black contours represent positive (negative) perturbation isotachs (contoured every $1\,\mathrm{m\,s^{-1}}$ with zero line removed). Gray contours show the 20 and $40\,\mathrm{m\,s^{-1}}$ isotachs of the model-mean 300-hPa zonal wind. (b) Homogeneous SST regression map (K). (c) Scatterplot of the wind and SST expansion coefficients.

coefficients is depicted in Fig. 8c and demonstrates their strong correlation. Therefore, the first pattern of co-variability identified by MCA appears robust and is shown in Fig. 8.

The patterns of covariability produced by MCA are depicted via regressing SST bias (homogeneous; Fig. 8b) and zonal wind bias (heterogeneous; Fig. 8a) onto the SST expansion coefficient. Regression onto the zonal wind expansion coefficient yields similar structures. Here, we focus on the SST expansion coefficient as a potential predictor of zonal wind bias as our leading hypothesis is that the tropical SST bias forces the zonal wind bias (further discussion found in section 4).

The homogeneous SST field (Fig. 8b) strongly re-sembles the positive phase of ENSO and exhibits a high spatial correlation with the reanalysis ENSO SST pattern, shown in Fig. 9b ($r = 0.66$), with further discussion to follow. The heterogeneous wind field (Fig. 8a) is similarly spatially correlated with the grouped model bias shown in Fig. 7 ($r = 0.78$). It is notable that ENSO-like SST biases are so directly connected to midlatitude jet biases through the first mode of covariability pro-duced by MCA. This indicates that the portrayal of the

winter mean state in the tropical Pacific affects the modeled upper-level midlatitude zonal winds in both the Pacific and Atlantic regions, suggesting that dif-ferences in NH jet stream portrayal among the 17 GCMs are associated with their respective representations of ENSO-like mean SST in the tropical Pacific. Again, we note that the causality is not established by the MCA; further discussion is found in section 4.

The open circles added to Fig. 6, seek to explain the relationship between the grouped model bias and the ENSO-like structure of tropical Pacific SST biases. The open circles show the values of the normalized pro-jection of the heterogeneous wind pattern in the Pacific basin (Fig. 8a) onto the primary and secondary modes of zonal wind variability from the reanalysis data (EOFs 1 and 2; Figs. 2a,c). Because of the nonsigned nature of MCA, the open circles show both possible sign conven-tions. The addition of these circles shows that the por-tion of the model wind bias caused by ENSO-like mean SST biases in the tropical Pacific falls along almost the same axis as the bias of the jet stream between models in the Pacific. This is consistent with the hypothesis that the uncertainties in winter-mean Pacific jet stream

a. UWND regressed onto CTI
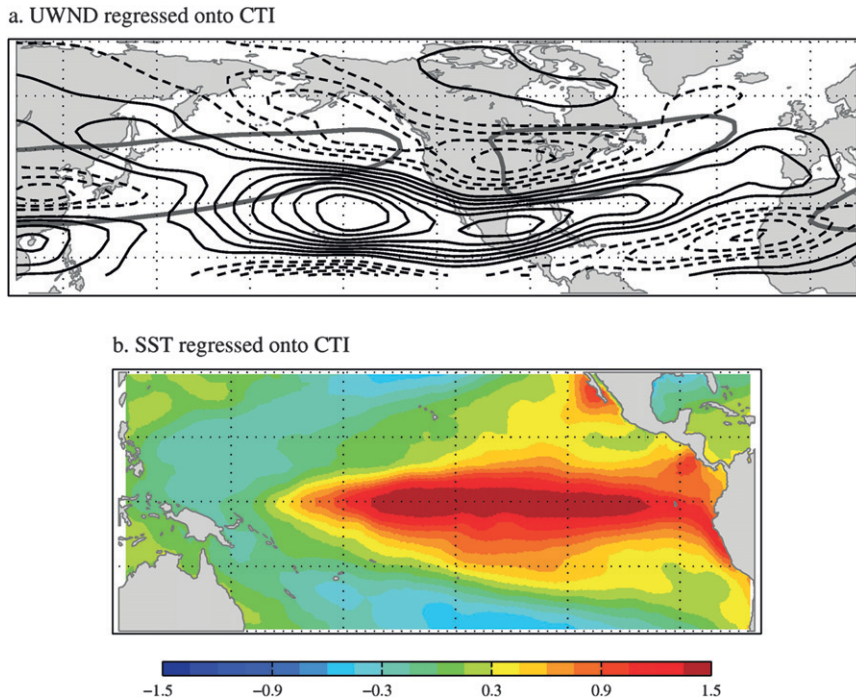

b. SST regressed onto CTI

FIG. 9. ENSO midlatitude wind teleconnection (1950–2009) shown by (a) observed winter-mean 300-hPa zonal wind regressed onto the winter-mean CTI. Solid (dashed) black contours represent positive (negative) perturbation isotachs (contoured every $0.5\,\mathrm{m\,s^{-1}}$ with zero line removed). Gray contours represent the 20 and $40\,\mathrm{m\,s^{-1}}$ isotachs of the mean 300-hPa zonal wind. (b) Winter-mean tropical Pacific SST regressed onto the winter-mean CTI (K).

portrayal are caused by each model's treatment of winter-mean tropical Pacific SST [consistent with Lau (1997), Trenberth et al. (1998), and Seager et al. (2003)] and suggests that if models produced a more consistent tropical Pacific winter-mean SST distribution, Pacific jet model biases might be more consistent. The same relationship is not as clear in the Atlantic, although it is noteworthy that the portion of zonal wind bias that is related to ENSO-like mean state biases (the circles in Fig. 6b) do generally align along the "group 1, group 2" axis. This suggests that tropical Pacific mean state biases may be responsible for some portion of the bias of the Atlantic jet as well.

To further confirm and detail the relationship of the Pacific modeled ENSO-like tropical mean state and midlatitude zonal wind biases, we examine the spatial structure of zonal wind variations associated with temporal ENSO variations in 60 years of reanalysis data, and compare these results with the results of the MCA above. One commonly used metric for defining ENSO is the cold tongue index (CTI; Zhang et al. 1997), defined by the SST anomaly pattern over the eastern equatorial Pacific (6°S–6°N, 180°–90°W). Figure 9 shows the regression of the reanalysis winter-average (NDJFM; annually resolved) zonal wind and winter-average SST fields

onto the reanalysis wintertime CTI for 1950–2009. The regression therefore represents the observed patterns of winter-average SST and upper-level zonal wind associated with a positive ENSO event. Figure 9b shows the canonical positive ENSO (El Niño) SST signal of warming in the eastern equatorial Pacific and Fig. 9a shows the wintertime zonal wind teleconnection pattern associated with positive ENSO SST anomalies. The positive phase of ENSO is associated with increased wind speeds within a subtropical band (15°–30°N) stretching from the date line to approximately 90°W. It is notable that the heterogeneous wind pattern shown in Fig. 8a has many similarities to the ENSO midlatitude wind teleconnection pattern from the reanalysis (Fig. 9a). Both patterns suggest a southward shift and strengthening of the equatorward flanks of the Pacific and Atlantic jets, characterized by a region of decreased winds north of the jet core and increased winds south of the jet core. These similarities are particularly apparent in the vicinity of the Pacific jet exit and Atlantic jet entrance regions.

The normalized projection of the reanalysis ENSO teleconnection pattern (Fig. 9a) onto the primary and secondary modes of variability from the reanalysis (EOFs 1 and 2; Figs. 2a,b) is shown by the open diamonds added
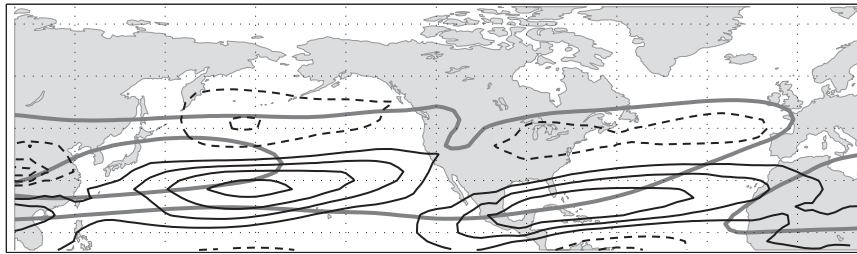
FIG. 10. 300-hPa zonal wind regressed onto the modeled winter-mean CTI for each model. Solid (dashed) black lines indicate positive (negative) perturbation isotachs (contoured every $1 \, m \, s^{-1}$ with zero line removed). Gray contours show the 20 and $40 \, m \, s^{-1}$ isotachs of the model-mean 300-hPa zonal wind.

to Fig. 6. In the Pacific region (Fig. 6a), these diamonds also fall along nearly the same axis as intermodel variations in jet stream biases and the heterogeneous wind pattern produced by MCA. The near alignment of these different variables shows that they all project onto a similar combination of EOFs 1 and 2. Thus, it is even more likely that the ENSO-like bias of modeled SSTs explains intermodel differences in the bias of NH jet streams in the Pacific. While the link between Atlantic jet biases and ENSO is weaker, intermodel variations do lie along the same axis as the ENSO teleconnection pattern. Therefore, it seems that model biases in the portrayal of the Atlantic jet are also affected by tropical Pacific SST mean state biases.

To further confirm the results of MCA, the winter-mean upper-level wind field is regressed onto the winter-mean CTI for each model, with results shown in Fig. 10. The results of this regression analysis look remarkably similar to the results of MCA, and are correlated with the heterogeneous wind field (Fig. 8a) at $r = 0.98$ and with the grouped model bias pattern (Fig. 7) at $r = 0.70$. This confirms that jet stream biases across the 17 GCMs are related to the ENSO-like biases in tropical Pacific SST in these models. However, a comparison between Figs. 10 and 9a shows that the jet stream bias pattern associated with ENSO-like SST biases in GCMs does not completely resemble the observed ENSO teleconnection pattern ($r = 0.57$). Additional thoughts on this issue are found in section 4.

One additional confirmation that the results of MCA are robust is an EOF/PC analysis of the winter-mean SST anomaly pattern across the 17 models. The primary mode of intermodel variability of the winter-mean SST anomaly pattern is well separated and explains 45% of the variance of SST across models. Figure 11 shows the regression of winter-mean zonal wind (Fig. 11a) and winter-mean SST (Fig. 11b) onto the primary mode of intermodel variability of SST. Both the wind (Fig. 11a) and the SST regression patterns (Fig. 11b) are highly

correlated with the heterogeneous wind pattern ($r = 0.77$) and homogeneous SST pattern ($r = 0.96$) from MCA, respectively.

To quantify how much intermodel variance is explained by the ENSO-like pattern identified by MCA, the SST expansion coefficient (i.e., the left singular vector) of the first mode of MCA covariability is used as a predictor of intermodel variance of winter-mean upper-level winds, allowing the determination of how much of the intermodel variance of upper-level winds is explained by GCM SST biases. The result of this analysis is shown in Fig. 12. Averaging the intermodel variance explained in Figs. 12a and 12b over the domain and calculating the total variance explained by mode 1 of MCA, we find that ENSO-like SST biases explain 21% of the total NH intermodel variance of midlatitude jet stream portrayal on average, with significantly more variance explained in the central subtropical Pacific and eastern subtropical Atlantic. Figure 12b shows that while SST biases do not explain all of the intermodel variance in upper-level winds, they do explain a fairly substantial portion, especially in the Pacific.

Further evidence of the relationship between tropical SST biases and midlatitude wind biases is shown in Fig. 13, which includes the winter-mean intermodel variance of upper-level midlatitude wind for 13 models from the Atmospheric Model Intercomparison Project (AMIP) and their corresponding coupled models (CMIP). Because of the availability of AMIP data, L'Institut Pierre-Simon Laplace Coupled Model, version 4 (IPSL-CM4; France); National Center for Atmospheric Research (NCAR) Community Climate System Model, version 3 (CCSM3; United States); NCAR Parallel Climate Model, version 1 (PCM1; United States); and the Hadley Centre Global Environmental Model, version 1 (HadGEM1; United Kingdom) were used [in place of INGV-SXG, CSIRO Mk3.0, CSIRO Mk3.5, BCCR-BCM2.0, CGCM3.1 (T63), CGCM3.1 (T47), ECHO-G, and GISS-AOM] in this analysis, resulting in slightly

a. UWND regressed onto PC1 SST
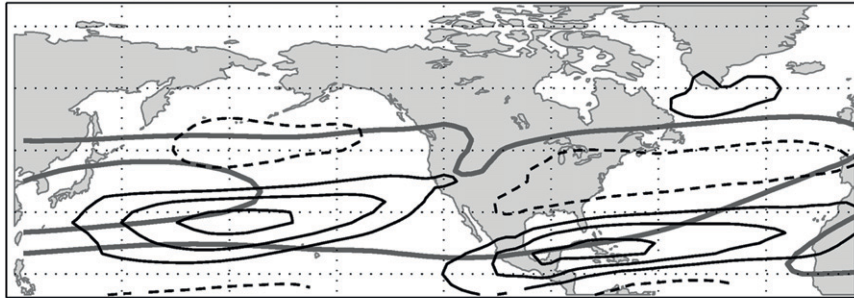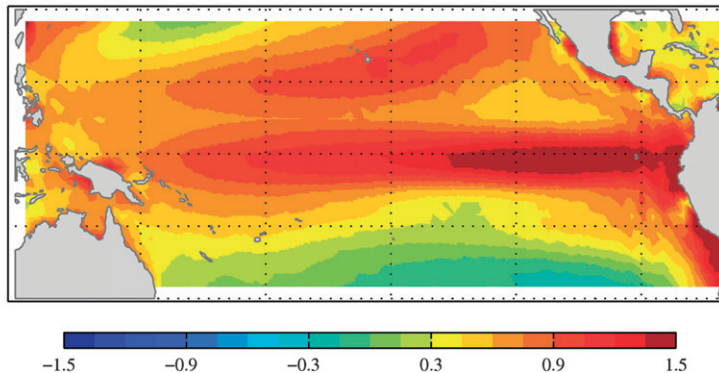

b. SST regressed onto PC1 SST

FIG. 11. (a) 300-hPa ensemble winter-mean zonal wind bias. Solid (dashed) black lines represent positive (negative) perturbation isotachs (contoured every $1 \, \mathrm{m \, s}^{-1}$ with zero line removed). Gray contours show the 20 and $40 \, \mathrm{m \, s}^{-1}$ isotachs of the 300-hPa ensemble winter-mean zonal wind, as in Fig. 4a. (b) Ensemble winter-mean tropical SST bias regressed onto the intermodel PC/EOF 1 of winter-mean tropical SST (K).

different intermodel variance in Fig. 13b than in Fig. 12a. However, the same 13 models are used in Figs. 13a and 13b. Note that the contour interval is different for Figs. 13a and 13b. As expected, the intermodel variance of winter-mean wind speed is smaller among the AMIP models than among the CMIP models, suggesting that the absence of ocean interactions decreases the variations of wind speed portrayal among the 13 GCMs. The intermodel variance decreases even more than that linked with ENSO-like SST biases in the current study (e.g., Fig. 12b), suggesting that other aspects of the ocean structure are impacting the midlatitude winter-mean wind biases in CMIP3 GCMs.

d. GCM portrayal of jet variability

To complete this analysis of NH jet stream portrayal, temporal variability of the upper-level winds is also considered. Given the relationship between the mean state of the jet and the structure of the variability, it is likely that a model's bias in jet structure will influence its representation of the variability. As such, we first characterize each model's variability via EOF/PC analysis,

compare the simulated variability to observed variability, and then evaluate the relationship between each model's simulated variability and its mean state bias.

First, the spatial structure of each model's jet variability is identified and compared with observations. Each model's primary and secondary modes of jet variability in the Pacific and Atlantic are identified via EOF/PC analysis, using the same methodology as used for the reanalysis data (section 3a). EOFs/PCs 1, 2, and 3 explain 19%, 13%, and 9% of the variance in the Pacific basin and 21%, 12%, and 9% of the variance in the Atlantic basin on average for the 17 GCMs. EOFs/PCs 1 and 2 are well separated for all models. The spatial structure of the resulting variability is compared with the spatial structure of the reanalysis in Fig. 14. Figure 14 shows the normalized projection of the first two EOFs of each model onto the first two EOFs of the reanalysis data (for the Pacific and Atlantic). Asterisks (crosses) indicate the value of the projection of EOF 1 (2) of a given model onto EOFs 1 and 2 of the reanalysis. For instance, an asterisk located at (1, 0) would describe an exemplary model's depiction of EOF 1 that is completely

a. Raw Inter–model Variance
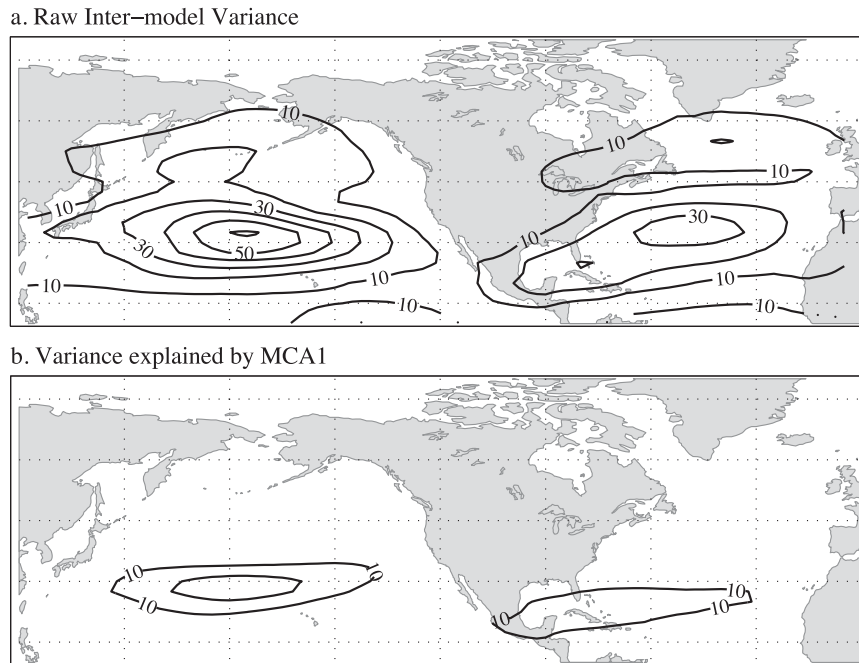

b. Variance explained by MCA1

FIG. 12. (a) Total intermodel variance of the winter-mean 300-hPa zonal wind and (b) intermodel variance of the winter-mean 300-hPa zonal wind explained by the SST expansion coefficient of the first mode of MCA covariability ($m^2\,s^{-2}$; CI: $10\,m^2\,s^{-2}$).

explained by reanalysis EOF 1 and not explained by reanalysis EOF 2. It is important to note that the sign of a given mode is arbitrary and therefore the polarity is assigned based upon the convention established by reanalysis EOFs 1 and 2 (Fig. 2).

Most projections cluster near $(0, 1)$ or $(1, 0)$, indicating that GCMs are successfully replicating the two dominant modes of variability. There is one outlier point for the Pacific. The Pacific outlier is EOF 2 from model 16 (GISS-ER) and indicates the reversal of EOFs 2 and 3 in that model (verified by visual inspection of the EOF spatial structures). Because EOFs 2 and 3 explain 10% and 9%, respectively, of the variability of the Pacific upper-level winds in GISS-ER, this reversal is not a serious flaw in the modeled variability. We have retained the projection on EOF 2 (the circled point near the origin in Fig. 14a) and have added the projection of GISS-ER EOF 3 (indicated with a diamond) to Fig. 14a. Therefore, all 17 models do a good job of replicating the two dominant modes of variability. Even the outlier has the correct structures represented in the wrong order. In fact, this variability appears more consistently replicated than the mean state of the jets in GCMs (Fig. 6).

At this point it is worth discussing the validity of our methodology for investigating jet variability and its relation to mean state biases. Our approach would likely not be appropriate if the mean state bias were so severe that it drastically altered the structure of the variability. Consider the case of a model with a jet that is drastically shifted poleward. The model may produce very realistic variability around its own jet, but the resulting EOFs may project very weakly onto the observed EOFs because of the poleward shift in their spatial structures. Perhaps the best justification that our approach is valid is that the projections of the models' EOFs onto the observed EOFs 1 and 2 are large, as shown in Fig. 14. Still, it is important to note that there could be subtle differences in the interpretation of the models' EOFs that could be illuminated by considering additional metrics (see, e.g., Barnes and Polvani 2013).

Next, we examine the relationship between the simulated variability and biases in model mean states. Because the location of the perturbation wind speeds associated with the dominant modes of variability is located nearby the jet exit region (see, e.g., Fig. 2), a measure of the longitude of the jet exit region and longitude of wind speed anomalies associated with EOFs 1 and 2 is used to find a functional relationship between jet mean state and variability. A regression analysis, shown in Fig. 15 examines the relationship between the modeled modes of variability and modeled mean state of the Atlantic and Pacific jets. The longitude of the maximum wind perturbation associated with EOFs 1 and 2

a. Inter–model Variance – AMIP
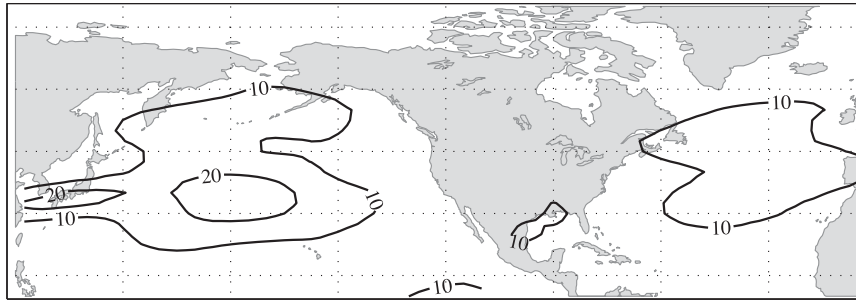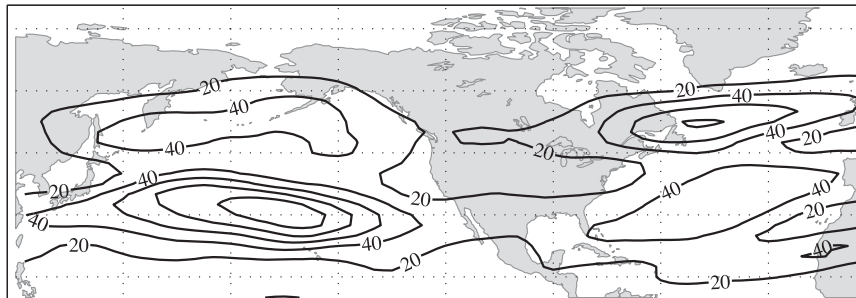

b. Inter–model Variance – CMIP

FIG. 13. (a) Total intermodel variance of the winter-mean 300-hPa zonal wind in 13 AMIP models (m^2 s^{-2}; CI: 10 m^2 s^{-2}) and (b) intermodel variance of the winter-mean 300-hPa zonal wind in the same models (m^2 s^{-2}; CI: 20 m^2 s^{-2}) (models listed in section 3c).

is regressed onto the longitude of the jet exit region for each model, as defined by the local minimum of the zonal gradient of the winter-mean zonal wind from each model. EOF 2 in model 16 (GISS-ER) is replaced by the model 16 EOF 3 in the Pacific (Fig. 15b, depicted with a diamond), consistent with the discussion of Fig. 14, above.

For the Pacific jet, the longitude of the maximum value of EOFs 1 and 2 is highly correlated with the longitude of the jet exit region ($r = 0.87$ and $r = 0.77$), shown in Figs. 15a and 15b (open circles show results from reanalysis dataset). For a sample size of 17, values of the correlation coefficient that exceed 0.48 are statistically significant at the 95% confidence level, based on the assumption of a two-tailed t test on the Pearson correlation coefficient. The $y = x$ line is also shown for the Pacific, which indicates the line the regression would follow if EOFs 1 and 2 were located exactly at the longitude of the jet exit region. Most models correctly portray the maximum wind perturbation to be located immediately downstream of the jet exit region. Figures 15c and 15d show the same analysis for the Atlantic jet, which does not display a similarly strong connection ($r = 0.57$ and $r = 0.32$), although the EOF 1 regression is statistically significant (and therefore the regression line is retained). Overall, there does not seem to be a link between the longitude of the mean state and variability for the Atlantic region, possibly because of the added complexity caused by the southwest–northeast tilt of the jet in this region.

There is a robust correspondence between the Pacific jet mean state and its variability, but not the Atlantic jet mean state and variability. When these results are repeated using GCM twenty-first-century A1B projections (not shown), this correspondence (or lack thereof in the Atlantic) does not change. Therefore, the Pacific jet exit region is critically related to the longitudinal position of EOFs/PCs 1 and 2, signifying that a correct characterization of the mean state of the Pacific jet stream may be vital to producing an accurate portrayal of the variability of that jet stream.

4. Conclusions

This study has focused on determining the reliability and robustness of nonzonally averaged NH jet stream portrayal in 17 GCMs from the CMIP3 dataset. This work is motivated by previous studies showing that GCM projections of twenty-first-century jet stream winds are related to biases in twentieth-century jet stream portrayal (Kidston and Gerber 2010). The results presented in this paper encourage targeted improvement of GCM jet stream portrayal, which is an important step toward assessing climate change impacts at a variety of scales.
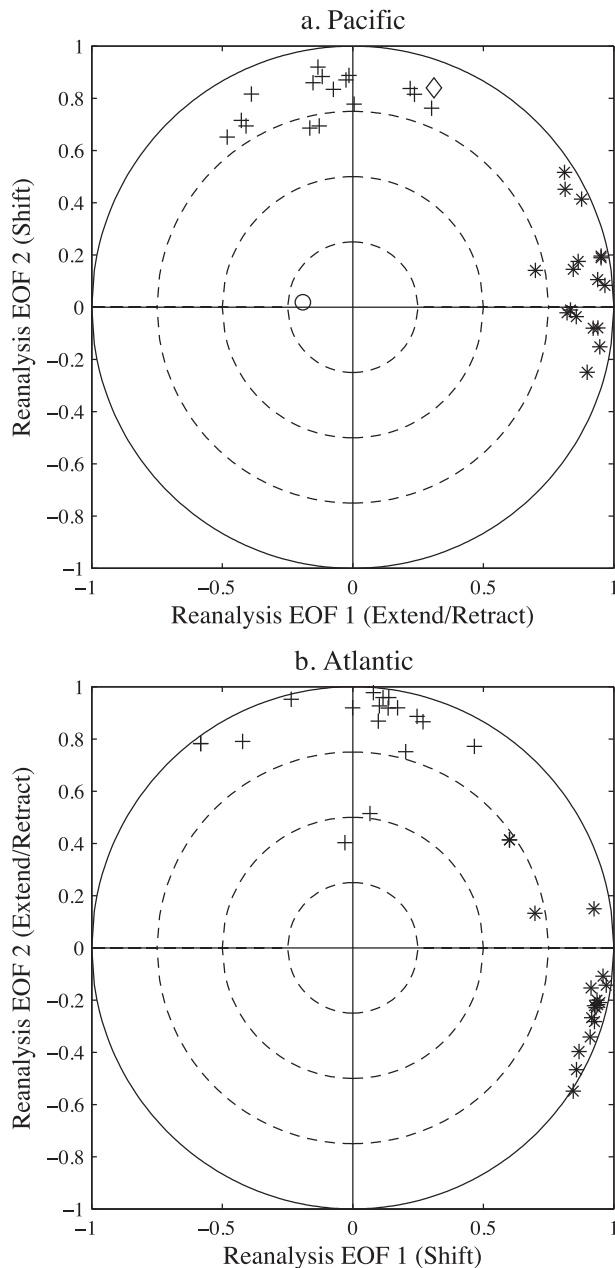
a. Pacific

b. Atlantic

FIG. 14. Scatterplot of the normalized projection of each model's EOFs/PCs 1 and 2 onto the corresponding reanalysis EOFs/PCs 1 and 2 for the (a) Pacific and (b) Atlantic. EOF 1 is indicated by asterisks (*) and EOF 2 is indicated by crosses (+). The circle (diamond) indicates EOF 2 (3) of model 16. Dashed circles indicate lines of constant correlation at $r = 0.25$, 0.5, and 0.75.

Examination of mean model biases of upper-level zonal winds suggests that the modeled Atlantic jet is too zonally extended and located too far equatorward relative to the reanalysis. The ensemble-mean Pacific jet has less bias than the Atlantic jet, but only because model agreement is much lower and biases in individual

models cancel in the ensemble mean. Winter-mean biases in both basins are significant relative to the variability of the upper-level zonal winds in reanalysis data.

MCA, EOF, and regression analysis are used separately to show that the NH biases in upper-level winds are strongly related to an ENSO-like pattern in winter-mean tropical Pacific SSTs. Throughout the analysis we have implicitly assumed that tropical SSTs are responsible for forcing midlatitude winds, suggesting that the variation in models' portrayal of the tropical Pacific mean state contributes to the bias of the midlatitude large-scale circulation. This hypothesis is consistent with prior research detailing ENSO teleconnection patterns (e.g., Lau 1997; Trenberth et al. 1998; Seager et al. 2003). There, ENSO-related SST variations cause shifts in atmospheric convection, which influence regions of upper-level convergence and divergence in the tropics. Regions of anomalous divergence and convergence provide a source for stationary Rossby wave propagation into the midlatitudes (Hoskins and Karoly 1981; Sardeshmukh and Hoskins 1988), including a deepening and eastward shift of the Aleutian low (and hence an equatorward shift and extension of the Pacific jet; Fig. 9). Although we have not explicitly diagnosed the causal relationship herein, we speculate that similar physical processes operate on the mean bias diagnosed in this study.

However, it is important to note that the reverse scenario is also possible. Recent studies have shown that variations in midlatitude and subtropical winds may also conspire to produce tropical Pacific ENSO variations, as evidenced by the seasonal footprinting mechanism examined in Vimont et al. (2001). It is possible that this causal mechanism (from midlatitude to the tropics) would also work in linking midlatitude wind biases to biases in tropical Pacific SST. While the present study does not resolve that causality, the similarity between the spatial structure of ENSO's teleconnection in the observed record to the model bias (Fig. 6a) and the comparison to AMIP GCM intermodel variability (Fig. 13) suggest that biases in the tropical Pacific are influencing midlatitude zonal wind biases. This hypothesized causality is also supported by recent findings that ocean circulation biases force biases in the North Atlantic storm track in climate model simulations (Woollings et al. 2012a).

The spatial structure of the leading modes of variability of the upper-level jet is found to be accurately simulated in nearly all 17 GCMs. Furthermore, it is shown that in the Pacific, biases that do exist in models' portrayal of EOFs 1 and 2 are strongly linked to the modeled longitude of the jet exit in the Pacific region. This result is particularly encouraging because it implies that an

EOF 1

a. Pacific (Extend/Retract)

EOF 2

b. Pacific (Shift)

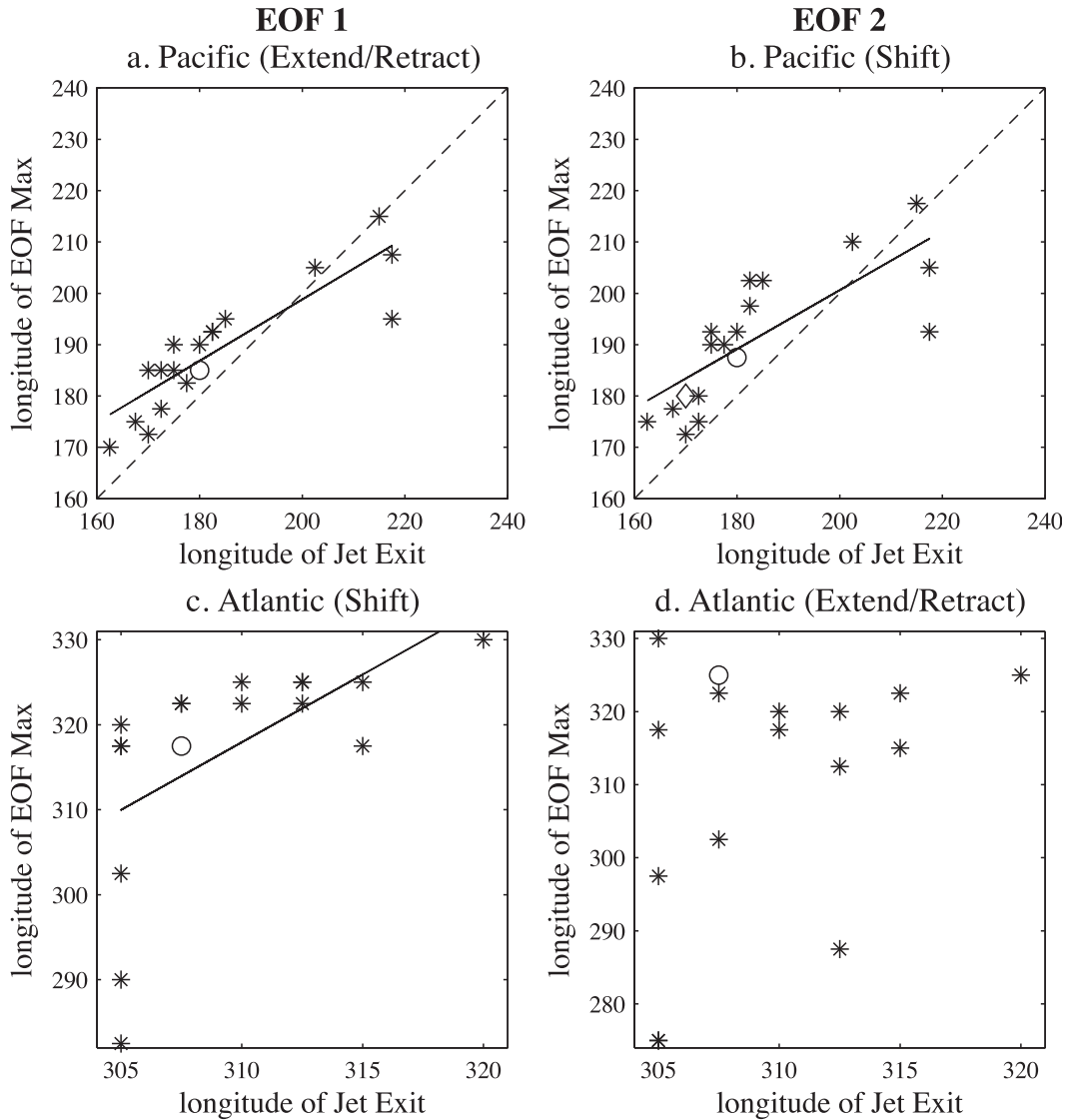## c. Atlantic (Shift)

d. Atlantic (Extend/Retract)

FIG. 15. Longitude of the max wind perturbation associated with EOFs 1 and 2 regressed onto the longitude of the jet exit region in each model for (a) Pacific EOF 1 (extend/retract), (b) Pacific EOF 2 (shift), (c) Atlantic EOF 1 (shift), and (d) Atlantic EOF 2 (extend/retract). Open circles represent reanalysis data and the dashed line shows $y = x$. The circle (diamond) in (b) indicates EOF 2 (3) of model 16. Longitudes are displayed in degrees east (e.g., 240°E = 120°W).

improved characterization of the mean state of the Pacific jet will also positively impact the modeled variability.

In conclusion, the results herein indicate that improvements in model portrayal of the tropical Pacific mean state may significantly advance the portrayal of the mean state of the Pacific and Atlantic jets, which will consequently improve the modeled jet stream variability in the Pacific. To complement these findings, a second paper (Delcambre et al. 2013) examines twenty-first-century GCM projections of the nonzonally averaged NH jet streams. Those results show that ENSO-like changes in the tropical Pacific mean state dominate

intermodel variations in projections of twenty-first-century NH jet streams.

for Climate Model Diagnosis and Intercomparison (PCMDI), and the WCRP's Working Group on Coupled Modelling (WGCM) for their roles in making available the WCRP CMIP3 multimodel dataset. Support of this dataset is provided by the Office of Science, U.S. Department of Energy.

REFERENCES

Athanasiadis, P., J. Wallace, and J. Wettstein, 2010: Patterns of wintertime jet stream variability and their relation to the storm tracks. *J. Atmos. Sci.,* **67,** 1361–1381.

Barnes, E., and L. Polvani, 2013: Response of the midlatitude jets and of their variability to increased greenhouse gases in the CMIP5 models. *J. Climate,* in press.

Bengtsson, L., K. Hodges, and E. Roeckner, 2006: Storm tracks and climate change. *J. Climate,* **19,** 3518–3543.

Bretherton, C., C. Smith, and J. Wallace, 1992: An intercomparison of methods for finding coupled patterns in climate data. *J. Climate,* **5,** 541–560.

Chang, E., S. Lee, and K. Swanson, 2002: Storm track dynamics. *J. Climate,* **15,** 2163–2183.

Chen, G., and I. Held, 2007: Phase speed spectra and the recent poleward shift of Southern Hemisphere surface westerlies. *Geophys. Res. Lett.,* **34,** L21805, doi:10.1029/2007GL031200.

Delcambre, S., D. Lorenz, D. Vimont, and J. Martin, 2013: Diagnosing Northern Hemisphere jet portrayal in 17 CMIP3 global climate models: Twenty-first-century projections. *J. Climate,* **26,** 4930–4946.

Delworth, T., and Coauthors, 2006: GFDL's CM2 global coupled climate models. Part I: Formulation and simulation characteristics. *J. Climate,* **19,** 643–674.

Deser, C., and M. Timlin, 1997: Atmosphere–ocean interaction on weekly timescales in the North Atlantic and Pacific. *J. Climate,* **10,** 393–408.

Eichelberger, S., and D. Hartmann, 2007: Zonal jet structure and the leading mode of variability. *J. Climate,* **20,** 5149–5163.

Flato, G., G. Boer, W. Lee, N. McFarlane, D. Ramsden, M. Reader, and A. Weaver, 2000: The Canadian Centre for Climate Modelling and Analysis of global coupled model and its climate. *Climate Dyn.,* **16,** 451–467.

Galin, V. Y., E. M. Volodin, and S. P. Smyshliaev, 2003: Atmosphere general circulation model of INM RAS with ozone dynamics. *Russ. Meteor. Hydrol.,* **5,** 13–22.

Gnanadesikan, A., and Coauthors, 2006: GFDL's CM2 global coupled climate models. Part II: The baseline ocean simulation. *J. Climate,* **19,** 675–697.

Gordon, H., and Coauthors, 2002: The CSIRO Mk3 Climate System Model. CSIRO Tech. Rep. 60, 130 pp.

Gualdi, S., E. Scoccimarro, A. Bellucci, A. Grezio, E. Manzini, and A. Navarra, 2006: The main features of the 20th century climate as simulated with the SXG coupled GCM. *Claris Newsletter,* No. 4, Centre National de la Recherche Scientifique, Paris, France, 7–13.

——, ——, and A. Navarra, 2008: Changes in tropical cyclone activity due to global warming: Results from a high-resolution coupled general circulation model. *J. Climate,* **21,** 5204–5228.

Hasumi, H., and S. Emori, 2004: K-1 coupled GCM (MIROC) description. K-1 Tech. Rep., Center for Climate System Research, University of Tokyo, 34 pp.

Hodges, K., 1994: A general method for tracking analysis and its application to meteorological data. *Mon. Wea. Rev.,* **122,** 2573–2586.

Hoskins, B., and D. Karoly, 1981: The steady linear response of a spherical atmosphere to thermal and orographic forcing. *J. Atmos. Sci.,* **38,** 1179–1196.

——, and P. Valdes, 1990: On the existence of storm-tracks. *J. Atmos. Sci.,* **47,** 1854–1864.

——, I. James, and G. White, 1983: The shape, propagation and mean-flow interaction of large-scale weather systems. *J. Atmos. Sci.,* **40,** 1595–1612.

Hu, Y., and Q. Fu, 2007: Observed poleward expansion of the Hadley circulation since 1979. *Atmos. Chem. Phys.,* **7,** 5229–5236.

Ihara, C., and Y. Kushnir, 2009: Change of mean midlatitude westerlies in 21st century climate simulations. *Geophys. Res. Lett.,* **36,** L13701, doi:10.1029/2009GL037674.

Jaffe, S., J. Martin, D. Vimont, and D. Lorenz, 2011: A synoptic climatology of episodic, subseasonal retractions of the Pacific jet. *J. Climate,* **24,** 2846–2860.

Johanson, C., and Q. Fu, 2009: Hadley cell widening: Model simulations versus observations. *J. Climate,* **22,** 2713–2725.

Jungclaus, J., and Coauthors, 2006: Ocean circulation and tropical variability in the coupled model ECHAM5/MPI-OM. *J. Climate,* **19,** 3952–3972.

Kalnay, E., and Coauthors, 1996: The NCEP/NCAR 40-Year Reanalysis Project. *Bull. Amer. Meteor. Soc.,* **77,** 437–471.

Karpechko, A., 2010: Uncertainties in future climate attributable to uncertainties in future northern annular mode trend. *Geophys. Res. Lett.,* **37,** L20702, doi:10.1029/2010GL044717.

Kidston, J., and E. Gerber, 2010: Intermodel variability of the poleward shift of the austral jet stream in the CMIP3 integrations linked to biases in 20th century climatology. *Geophys. Res. Lett.,* **37,** L09708, doi:10.1029/2010GL042873.

——, G. Vallis, S. Dean, and J. Renwick, 2011: Can the increase in the eddy length scale under global warming cause the poleward shift of the jet streams? *J. Climate,* **24,** 3764–3780.

Kushner, P., I. Held, and T. Delworth, 2001: Southern Hemisphere atmospheric circulation response to global warming. *J. Climate,* **14,** 2238–2249.

Lau, N.-C., 1997: Interactions between global SST anomalies and the midlatitude atmospheric circulation. *Bull. Amer. Meteor. Soc.,* **78,** 21–33.

Li, C., and J. Wettstein, 2012: Thermally driven and eddy-driven jet variability in reanalysis. *J. Climate,* **25,** 1587–1596.

Lorenz, D., and D. Hartmann, 2003: Eddy–zonal flow feedback in the Northern Hemisphere winter. *J. Climate,* **16,** 1212–1227.

——, and E. DeWeaver, 2007: Tropopause height and zonal wind response to global warming in the IPCC scenario integrations. *J. Geophys. Res.,* **112,** D10119, doi:10.1029/2006JD008087.

Lu, J., G. Vecchi, and T. Reichler, 2007: Expansion of the Hadley cell under global warming. *Geophys. Res. Lett.,* **34,** L06805, doi:10.1029/2006GL028443.

Lucarini, V., and G. Russell, 2002: Comparison of mean climate trends in the Northern Hemisphere between National Centers for Environmental Prediction and two atmosphere–ocean model forced runs. *J. Geophys. Res.,* **107** (D15), doi:10.1029/2001JD001247.

Marshall, G., 2003: Trends in the southern annular mode from observations and reanalyses. *J. Climate,* **16,** 4134–4143.

Meehl, G., C. Covey, T. Delworth, M. Latif, B. McAvaney, J. Mitchell, R. Stouffer, and K. Taylor, 2007: The WCRP CMIP3 multimodel dataset: A new era in climate change research. *Bull. Amer. Meteor. Soc.,* **88,** 1383–1394.

North, G., T. Bell, R. Cahalan, and F. Moeng, 1982: Sampling errors in the estimation of empirical orthogonal functions. *Mon. Wea. Rev.,* **110,** 699–706.

Orlanski, I., 1998: Poleward deflection of storm tracks. *J. Atmos. Sci.,* **55,** 2577–2602.

Overland, J., and M. Wang, 2005: The Arctic climate paradox: The recent decrease of the Arctic Oscillation. *Geophys. Res. Lett.,* **32,** L06701, doi:10.1029/2004GL021752.

Russell, G., J. Miller, and D. Rind, 1995: A coupled atmosphere– ocean model for transient climate change studies. *Atmos.– Ocean,* **33,** 683–730.

Sardeshmukh, P., and B. Hoskins, 1988: The generation of global rotational flow by steady idealized tropical divergence. *J. Atmos. Sci.,* **45,** 1228–1251.

Schmidt, G., and Coauthors, 2006: Present-day atmospheric simulations using GISS ModelE: Comparison to in situ, satellite, and reanalysis data. *J. Climate,* **19,** 153–192.

Seager, R., N. Harnik, Y. Kushnir, W. Robinson, and J. Miller, 2003: Mechanisms of hemispherically symmetric climate variability. *J. Climate,* **16,** 2960–2978.

Simmons, A., J. Wallace, and G. Branstator, 1983: Barotropic wave propagation and instability, and atmospheric teleconnection patterns. *J. Atmos. Sci.,* **40,** 1363–1392.

Solomon, S., D. Qin, M. Manning, M. Marquis, K. Averyt, M. M. B. Tignor, H. L. Miller Jr., and Z. Chen, Eds., 2007: *Climate Change 2007: The Physical Science Basis.* Cambridge University Press, 996 pp.

Thompson, D., and J. Wallace, 2000: Annular modes in the extratropical circulation. Part I: Month-to-month variability. *J. Climate,* **13,** 1000–1016.

——, ——, and G. Hegerl, 2000: Annular modes in the extratropical circulation. Part II: Trends. *J. Climate,* **13,** 1018– 1036.

Trenberth, K., G. Branstator, D. Karoly, N.-C. Lau, and C. Ropelewski, 1998: Progress during TOGA in understanding and modeling global teleconnections associated with tropical sea surface temperatures. *J. Geophys. Res.,* **103** (C7), 14 291–14 324.

Ulbrich, U., J. Pinto, H. Kupfer, G. Leckebusch, T. Spangehl, and M. Reyers, 2008: Changing Northern Hemisphere storm tracks in an ensemble of IPCC climate change simulations. *J. Climate,* **21,** 1669–1679.

Valdes, P., and B. Hoskins, 1989: Linear stationary wave simulations of the time-mean climatological flow. *J. Atmos. Sci.,* **46,** 2509–2527.

Vimont, D., D. Battisti, and A. Hirst, 2001: Footprinting: A seasonal connection between the tropics and mid-latitudes. *Geophys. Res. Lett.,* **28,** 3923–3926.

Volodin, E., and N. Diansky, 2004: El Niño reproduction in a coupled general circulation model of atmosphere and ocean. *Russ. Meteor. Hydrol.,* **12,** 5–14.

Wallace, J., C. Smith, and C. Bretherton, 1992: Singular value decomposition of wintertime sea surface temperature and 500-mb height anomalies. *J. Climate,* **5,** 561–576.

Wettstein, J., and J. Wallace, 2010: Observed patterns of month-to- month storm-track variability and their relationship to the background flow. *J. Atmos. Sci.,* **67,** 1420–1437.

Woollings, T., 2008: Vertical structure of anthropogenic zonal- mean atmospheric circulation change. *Geophys. Res. Lett.,* **35,** L19702, doi:10.1029/2008GL034883.

——, and M. Blackburn, 2012: The North Atlantic jet stream under climate change, and its relation to the NAO and EA patterns. *J. Climate,* **25,** 886–902.

——, J. Gregory, J. Pinto, M. Reyers, and D. Brayshaw, 2012a: Response of the North Atlantic storm track to climate change shaped by ocean–atmosphere coupling. *Nat. Geosci.,* **5,** 313– 317, doi:10.1038/ngeo1438.

——, A. Hannachi, and B. Hoskins, 2012b: Variability of the North Atlantic eddy-driven jet stream. *Quart. J. Roy. Meteor. Soc.,* **136,** 856–868.

Wu, Y., M. Ting, R. Seager, H. Huang, and M. Cane, 2010: Changes in storm tracks and energy transports in a warmer climate simulated by the GFDL CM2.1 model. *Climate Dyn.,* **37,** 53–72.

Yaocun, Z., and H. Daqing, 2011: Has the East Asian westerly jet experienced a poleward displacement in recent decades? *Adv. Atmos. Sci.,* **28,** 1259–1265.

Yin, J., 2005: A consistent poleward shift of the storm tracks in simulations of 21st century climate. *Geophys. Res. Lett.,* **32,** L18701, doi:10.1029/2005GL023684.

Yu, Y., R. Yu, X. Zhang, and H. Liu, 2002: A flexible coupled ocean–atmosphere general circulation model. *Adv. Atmos. Sci.,* **19,** 169–190.

——, X. Zhang, and Y. Guo, 2004: Global coupled ocean– atmosphere general circulation models in LASG/IAP. *Adv. Atmos. Sci.,* **21,** 444–455.

Yukimoto, S., and Coauthors, 2006: Present-day climate and climate sensitivity in the Meteorological Research Institute coupled GCM version 2.3 (MRI-CGCM2.3). *J. Meteor. Soc. Japan,* **84,** 333–363.

Zhang, Y., J. Wallace, and D. Battisti, 1997: ENSO-like interdecadal variability: 1900–93. *J. Climate,* **10,** 1004–1020.